

Resonant tunneling of electrons in AlSb/GaInAsSb double barrier quantum wells

Cite as: AIP Advances **10**, 055024 (2020); <https://doi.org/10.1063/5.0008959>

Submitted: 26 March 2020 • Accepted: 06 May 2020 • Published Online: 21 May 2020

 Edgar David Guarin Castro, Florian Rothmayr, Sebastian Krüger, et al.



View Online



Export Citation



CrossMark

ARTICLES YOU MAY BE INTERESTED IN

[Band parameters for III-V compound semiconductors and their alloys](#)

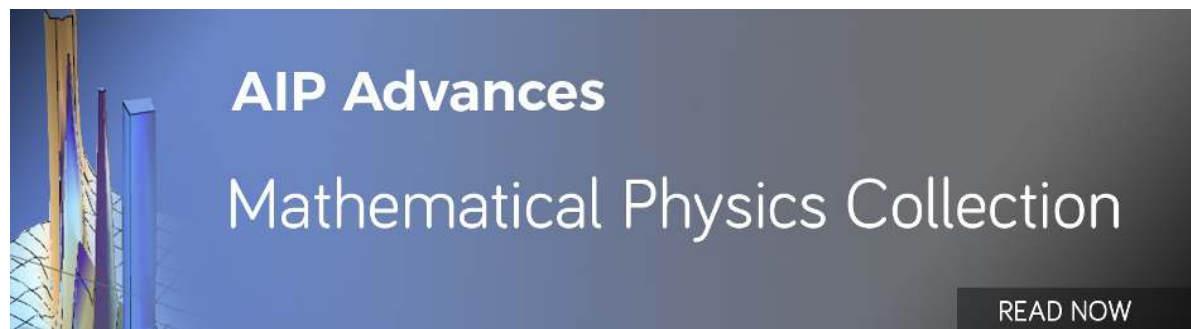
Journal of Applied Physics **89**, 5815 (2001); <https://doi.org/10.1063/1.1368156>

[Resonant tunneling in semiconductor double barriers](#)

Applied Physics Letters **24**, 593 (1974); <https://doi.org/10.1063/1.1655067>

[Tunneling in a finite superlattice](#)

Applied Physics Letters **22**, 562 (1973); <https://doi.org/10.1063/1.1654509>



AIP Advances
Mathematical Physics Collection

READ NOW

Resonant tunneling of electrons in AlSb/GaInAsSb double barrier quantum wells

Cite as: AIP Advances 10, 055024 (2020); doi: 10.1063/5.0008959

Submitted: 26 March 2020 • Accepted: 6 May 2020 •

Published Online: 21 May 2020



Edgar David Guarin Castro,^{1,2} Florian Rothmayr,^{1,3} Sebastian Krüger,¹ Georg Knebl,¹ Anne Schade,¹ Johannes Koeth,³ Lukas Worschech,¹ Victor Lopez-Richard,² Gilmar Eugenio Marques,² Fabian Hartmann,^{1,a)} Andreas Pfenning,^{1,b)} and Sven Höfling¹

AFFILIATIONS

¹Technische Physik, Physikalisches Institut and Röntgen Center for Complex Material Systems (RCCM), Universität Würzburg, Am Hubland, D-97074 Würzburg, Germany

²Departamento de Física, Universidade Federal de São Carlos, 13565-905 São Carlos, SP, Brazil

³nanoplus Nanosystems and Technologies GmbH, Oberer Kirschberg 4, D-97218 Gerbrunn, Germany

^{a)}Email: Fabian.Hartmann@physik.uni-wuerzburg.de

^{b)}Author to whom correspondence should be addressed: Andreas.Pfenning@physik.uni-wuerzburg.de

ABSTRACT

We have studied the optical and electronic transport properties of *n*-type AlSb/GaInAsSb double barrier quantum well resonant tunneling diodes (RTDs). The RTDs were grown by molecular beam epitaxy on GaSb substrates. Collector, quantum well, and emitter regions are comprised of the lattice-matched quaternary semiconductor Ga_{0.64}In_{0.36}As_{0.33}Sb_{0.67}. Photoluminescence emission spectra reveal a direct bandgap semiconductor with a bandgap energy of $E_g \approx 0.37$ eV, which corresponds to a cut-off wavelength of $\lambda \approx 3.3$ μm . The composition-dependent bandgap energy is found to follow Shim's model. At room temperature, we observe resonance current densities of $j_{res} = 0.143$ kA cm^{-2} with peak-to-valley current ratios of up to $PVCR = 6.2$. At cryogenic temperatures $T < 50$ K, the peak-to-valley current ratio increases up to $PVCR = 16$.

© 2020 Author(s). All article content, except where otherwise noted, is licensed under a Creative Commons Attribution (CC BY) license (<http://creativecommons.org/licenses/by/4.0/>). <https://doi.org/10.1063/5.0008959>

From optical molecule and gas spectroscopy,¹⁻³ optical coherence tomography (OCT), and light detection and ranging (LiDAR)^{4,5} to photonic quantum information technology,^{6,7} there has been an increasing demand for high-performance optoelectronic devices in the mid-infrared (MIR) spectral region above wavelengths of $\lambda \geq 2$ μm .⁸ Providing a huge variety of bandgap energies and band alignments, the so-called 6.1-Å family (InAs, GaSb, AlSb, and compounds) has been the material system of choice for semiconductor devices covering the MIR.⁹⁻¹⁴ In this regard, the quaternary compound GaInAsSb with its widely tunable direct bandgap has been routinely used as an optically active material. Recent examples of GaInAsSb as an optically active material include vertical cavity surface-emitting lasers,¹⁵ as well as more-elaborate schemes, such as interband cascade photodetectors¹⁶ or interband cascade lasers.^{17,18} Besides being employed as an optically active material, GaInAsSb brings a variety of promising properties to be applied

in electric devices. Compared to GaSb, the residual hole concentration caused by intrinsic *p*-type doping disappears for increasing In concentrations.¹⁹ L-valley occupation is negligible except for high doping concentrations exceeding $n \gg 1 \times 10^{18}$ cm^{-3} , due to the higher Γ -L energy separation in the conduction band.²⁰ As a result, for similar doping concentrations, both electron density and mobility are increased in GaInAsSb,²¹ at significantly lower specific contact resistivities.^{21,22} One such electronic device that could benefit from using GaInAsSb is the double barrier quantum well (DBQW) resonant tunneling diode (RTD).²³⁻²⁵ DBQW RTDs can be considered an ideal testbed to investigate quantum transport and heterostructure material parameters,²⁶ e.g., to optimize more complex structures, such as quantum cascade lasers as suggested in Ref. 27. Here, we present a thorough study on the electronic transport properties of AlSb/GaInAsSb DBQW RTDs grown by molecular beam epitaxy.

Design options of AlSb double barrier quantum well resonant tunneling diodes comprising the quaternary semiconductor GaInAsSb as emitter, quantum well, and collector material are shown in Fig. 1. Figures 1(a) and 1(b) provide band profile sketches of AlSb/InAs and AlSb/GaSb DBQW RTDs, respectively. The valence band (VB) maximum is depicted as a solid blue line, the Γ -point conduction band (CB) minimum as a solid black line, and the L-point CB minimum as a dashed red line. These two structures represent the well-studied limits that can be covered by changing the GaInAsSb composition. In particular, the low effective electron mass in InAs in conjunction with the high AlSb CB barrier height of $E_b \cong 2$ eV enables outstanding RTD device characteristics for high-frequency applications and oscillator circuits.^{28–30} On the other hand (literally speaking in this figure), AlSb/GaSb RTDs have been mainly studied for their peculiar transport channels originating from the close energetic proximity of L- and Γ -point,^{31,32} or as photodetectors for the mid-infrared spectral region (enabled by the pronounced type-I band alignment).^{33–35}

Hence, RTDs comprising GaInAsSb could combine the excellent transport properties of InAs-based devices with the optoelectronic capabilities of GaSb-based RTDs. Figure 1(c) shows the evolution of the conduction and valence band edge of lattice-matched $(\text{GaSb})_x(\text{InAs}_{0.91}\text{Sb}_{0.09})_{1-x}$ as a function of composition x after Shim (see Ref. 36). By choosing the appropriate composition x , the optical and electronic properties defining an RTD, such as barrier height (2 eV $\geq E_b \geq 1$ eV), bandgap energy (0.2 eV $\leq E_g \leq 0.7$ eV), and Γ -L energy separation (0.7 eV $\geq \Delta E_{\Gamma-L} \geq 25$ meV), can be tuned across a wide range.

The RTD layout and the fundamental optical and electronic properties are shown in Fig. 2. A cross-sectional scanning electron microscopy (SEM) image of the grown RTD sample is shown in Fig. 2(a). The RTD is grown by means of molecular beam epitaxy (MBE) on an n -type Te-doped GaSb substrate. The MBE chamber is equipped with solid-state evaporation cells for the group-III elements and dopants. Group-V elements are provided by valved cracking cells. The sample growth starts with 300 nm n -type Te-doped

GaSb with a doping concentration of $n = 2 \times 10^{18} \text{ cm}^{-3}$ followed by 120 nm of n -type GaSb with $n = 1 \times 10^{18} \text{ cm}^{-3}$. Subsequently, 195 nm of lattice-matched $\text{Ga}_{0.64}\text{In}_{0.36}\text{As}_{0.33}\text{Sb}_{0.67}$ are grown. This material composition is chosen due to its bandgap energy of $E_g = 374$ meV [see calibration series in Fig. 2(b)], which covers CH_4 , NO_2 , and NH_3 absorption lines,³⁷ and marks the optimal Interband Cascade Laser (ICL) operation region.¹³ During the first 170 nm, the doping concentration is reduced from $n = 5 \times 10^{17} \text{ cm}^{-3}$ to $n = 1 \times 10^{17} \text{ cm}^{-3}$. The subsequent 25 nm are intentionally left undoped. The DBQW is comprised of two 4 nm wide AlSb barriers sandwiching a 5 nm wide $\text{Ga}_{0.64}\text{In}_{0.36}\text{As}_{0.33}\text{Sb}_{0.67}$ quantum well. The following 25 nm of $\text{Ga}_{0.64}\text{In}_{0.36}\text{As}_{0.33}\text{Sb}_{0.67}$ are again undoped, followed by 200 nm of $\text{Ga}_{0.64}\text{In}_{0.36}\text{As}_{0.33}\text{Sb}_{0.67}$ with increasing doping concentration from $n = 1 \times 10^{17} \text{ cm}^{-3}$ to $n = 5 \times 10^{17} \text{ cm}^{-3}$. The heterostructure is finalized by 170 nm of heavily n -type doped GaSb with $n = 1 \times 10^{18} \text{ cm}^{-3}$. The doping profile is examined and confirmed by time-of-flight secondary ion mass spectroscopy (TOF-SIMS). Cross-sectional SEM is performed to confirm crystal growth rates and heterostructure thicknesses. Areas with dark contrast represent regions with high Al concentration, which allows us to precisely determine the position of the AlSb/GaInAsSb DBQW, whereas the GaInAsSb and GaSb regions can only be distinguished by their interface.

To investigate the fundamental bandgap energy of GaInAsSb lattice-matched to GaSb, we had measured a calibration series ranging from $x = 0.88$ up to $x = 0.64$ via photoluminescence (PL) via Fourier-transform infrared (FTIR) spectroscopy. The normalized room temperature PL spectra are shown in Fig. 2(b) on a logarithmic scale. Because the PL spectra are measured in ambient air conditions, they can be subject to water absorption lines present between 435 meV up to 490 meV (see HITRAN 2016 database).³⁷ The high-energy side of the spectra follows Boltzmann's distribution function as indicated by the red dashed line [$\propto \exp(-h\nu/(k_B T))$, with k_B as the Boltzmann constant, T as the temperature, h as the Planck constant, and ν as the photon frequency]. The exponential decay of 25 meV corresponds to charge carrier thermalization at room temperature. The low-energy side of the PL spectra is determined by

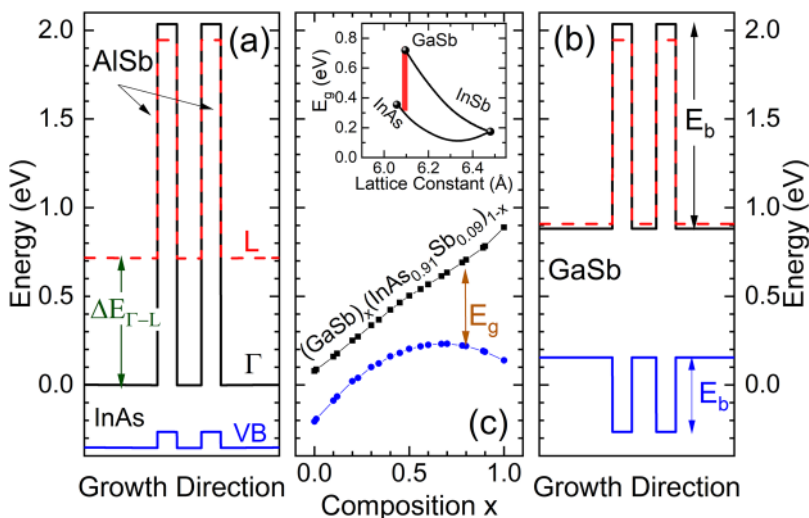


FIG. 1. Design options of AlSb/GaInAsSb resonant tunneling diodes. (a) Band profile sketch of the AlSb/InAs double barrier quantum well (DBQW) resonant tunneling structure. Valence band (VB) maximum and the conduction band (CB) minima at the Γ - and L-point are shown as blue, black, and red dashed lines, respectively. (b) Band profile sketch of the AlSb/GaSb DBQW RTD. (c) Conduction and valence band edge of lattice-matched $(\text{GaSb})_x(\text{InAs}_{0.91}\text{Sb}_{0.09})_{1-x}$ as a function of composition x as reported in Ref. 36. The inset illustrates the bandgap energy vs lattice constant for the binary semiconductors GaSb, InAs, and InSb, as well as their ternary alloys. The thick red line highlights the bandgap energies that can be covered with $(\text{GaSb})_x(\text{InAs}_{0.91}\text{Sb}_{0.09})_{1-x}$.

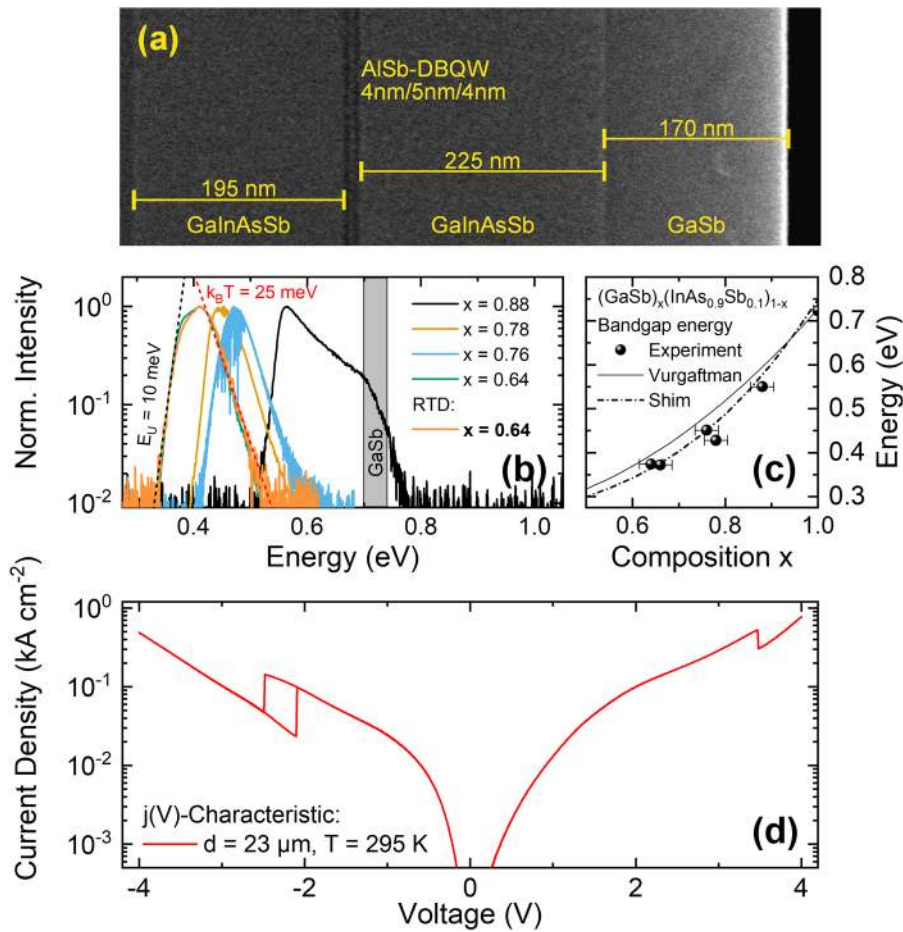


FIG. 2. RTD device layout and fundamental properties. (a) Cross-sectional scanning electron microscopy image of the grown RTD. (b) Photoluminescence spectra for lattice-matched $(\text{GaSb})_x(\text{InAs}_{0.91}\text{Sb}_{0.09})_{1-x}$ with different compositions x . The orange line for $x = 0.64$ is the spectrum of the studied RTD. The gray shaded region marks the influence of the surrounding GaSb. (c) Bandgap energy vs composition x . Experimentally determined bandgap energies are depicted as black spheres. The models after Vurgaftman *et al.* (Ref. 42) and Shim (Ref. 36) are shown as solid and dashed black lines, respectively. (d) Room temperature current density-voltage characteristic of a diode with diameter $d = 23 \mu\text{m}$.

Urbach's rule.³⁸ Due to the formation of a band tail, photons with an energy lower than the fundamental bandgap energy ($h\nu < E_g$) can be emitted. The emission intensity is proportional to $\propto \exp(h\nu/E_U)$, where E_U is the Urbach parameter, a measure of the thermal and structural disorder within a semiconductor material.^{38,39} For the RTD sample ($x = 0.64$, orange line), an Urbach parameter of $E_U = 10 \text{ meV}$ is determined, which is identical to the value we recently reported for MBE-grown p -type GaInAsSb,³⁵ and it compares well with the values previously reported for GaInAsSb grown by liquid phase epitaxy.⁴⁰ The small E_U and thermalized charge carrier distribution both indicate excellent sample quality. Furthermore, the single emission peaks show no indication of phase separation. Indeed, it has been demonstrated that phase-separation can be suppressed throughout the miscibility gap by choosing appropriate MBE growth conditions.⁴¹

The bandgap energy is extracted from the PL emission spectra as the low-energy side spectral position, at which the emission intensity has dropped to half its maximum. These values coincide well with the spectral position, at which the emission line starts to deviate from the exponential Urbach fit function. In Fig. 2(c), the bandgap energy is plotted as a function of the composition x . The dashed line represents the bandgap energy reported by Shim,³⁶

whereas experimentally obtained values are shown as black spheres. While the exact composition of ternary semiconductors can be precisely resolved by high-resolution x-ray diffraction (HR-XRD), this is not the case for lattice-matched quaternaries, since substrate and quaternary diffraction peaks coincide. Instead, the exact composition is achieved by an iterative two-step process. The group-III composition is precisely tuned via Ga and In growth rates. Lattice-matched growth is achieved via the group-V flux ratio and confirmed by HR-XRD. We estimate a residual composition uncertainty of about $\pm 2\%$. Within this uncertainty, we can reproduce the values by Shim's model, whereas the bowing parameter suggested by Vurgaftman *et al.* seems to slightly overestimate the bandgap energy by about $\sim 35 \text{ meV}$.^{36,42} On a closer look, Vurgaftman *et al.* reported a trend toward a higher bowing parameter, which is supported by our results. For the RTD sample ($x = 0.64$), a bandgap energy of $E_g = 0.376 \text{ eV}$ is found (corresponding to a cut-off wavelength of $\lambda \cong 3.3 \mu\text{m}$).

After confirmation of the excellent sample quality via PL spectroscopy, RTD device fabrication is initiated. Circular RTD mesa structures with diameters $d = 16 \mu\text{m}$ up to $d = 121 \mu\text{m}$ are processed via optical lithography and reactive ion etching. The mesa diameter is checked via optical microscopy. A $\text{Si}_3\text{N}_4/\text{SiO}_2$ passivation is

deposited via sputtering for sidewall leakage reduction. AuGe/Ni/Au is deposited as bottom contact on the substrate side. On top of the RTD mesa structure, galvanic deposition is used to form ohmic Ti/Pt/Au ring-shaped contacts. To study the electronic transport properties, the current–voltage [$I(V)$] characteristics are measured in the dark. The corresponding current density–voltage [$j(V)$] characteristics are obtained from the $I(V)$ and the diode area. Figure 2(d) shows the room temperature $j(V)$ characteristic of an RTD with $d = 23 \mu\text{m}$ plotted on a logarithmic scale. Following the symmetric heterostructure design, we observe a symmetric RTD $j(V)$ characteristic with pronounced resonances confirming resonant tunneling of electrons. For negative bias voltages (injection from the ring-contact side), the resonance current density is found to be $j_{\text{res}} = 143 \text{ A cm}^{-2}$ at a voltage of $V_{\text{res}} = -2.46 \text{ V}$. The valley current density is $j_{\text{val}} = 23 \text{ A cm}^{-2}$ at $V_{\text{val}} = -2.10 \text{ V}$. The corresponding peak-to-valley current ratio is $PVCR = 6.2$, which marks a significant improvement over previously reported values: $PVCR = 2.36$ for AlSb/GaSb RTDs employing ternary prewell emitter structures⁴³ and $PVCR = 4.3$ for AlSb/GaSb RTD photodetectors with absorption layer charge carrier injection.^{34,44} However, $PVCR = 11$ for AlSb/InAs RTDs as reported by Söderström *et al.* is not reached.³⁰ For positive voltages (injection from the substrate side), a resonance of $j_{\text{res}} = 520 \text{ A cm}^{-2}$ is found at $V = 3.47 \text{ V}$. Particularly $j_{\text{val}} = 305 \text{ A cm}^{-2}$ is significantly increased, resulting in a $PVCR = 1.7$. For larger diameters, the current resonance decreases and disappears completely. Hence, we ascribe the reduced PVCR at positive voltages to inhomogeneous current spreading caused by the ring-shaped contacts.

To investigate reproducibility and possible issues of, e.g., surface leakage in our samples, the $I(V)$ characteristics are taken for different diodes with $d = 16 \mu\text{m}$ up to $d = 121 \mu\text{m}$. Figure 3 shows the diode area dependence of the electronic transport properties. In Fig. 3(a), three exemplary $j(V)$ characteristics for $d = 23 \mu\text{m}$ (black), $d = 44 \mu\text{m}$ (orange), and $d = 51 \mu\text{m}$ (blue) are shown. For all measured $I(V)$ characteristics, resonance current (I_{res}) and valley current (I_{val}) are determined and shown as a function of the diode area

$A_{\text{RTD}} = \pi \cdot (d/2)^2$ in Fig. 3(b) as black and red dots, respectively. For better comparison, the resonance and valley currents are extrapolated ($I = j \cdot A_{\text{RTD}}$) from the best measured device ($d = 23 \mu\text{m}$, $j_{\text{res}} = 143 \text{ A cm}^{-2}$, $j_{\text{val}} = 23 \text{ A cm}^{-2}$, and $PVCR = 6.2$). Despite a seemingly linear increase with the diode area, both I_{res} and I_{val} increasingly deviate from their respective ideal lines. For increasing A_{RTD} , I_{res} falls increasingly short of its ideal value as indicated by the dashed black line, while I_{val} increasingly exceeds its ideal value. As a result, the PVCR drops from $PVCR \approx 6$ for the smallest diameters to about $PVCR \approx 3.5$ measured for the diodes with the largest areas [see Fig. 3(c)]. Typically, one would assume the PVCR to increase with increasing diode area and approach a constant value as surface defects and sidewall leakage become less dominant.^{34,45–47} Sidewall leakage seems to be negligible, however, an in-detail area/perimeter study (as executed, e.g., in Ref. 47, and ideally with smaller diameter diodes) would be necessary to unambiguously make that distinction. Instead, we assume an increasingly inhomogeneous current spreading from the top ring-contact to be the mechanism reducing the PVCR.

Figure 4 shows the temperature dependence of resonant tunneling in AlSb/GaInAsSb DBQW RTDs. $I(V)$ characteristics are measured at different temperatures between $T = 4.2 \text{ K}$ and room temperature ($T = 295 \text{ K}$). The experiment is conducted in a helium cryostat connected to a proportional-integral-derivative (PID) temperature controller. Temperature sensor and RTD are located at slightly different positions within the cryostat. To account for temperature deviations between sensor and sample, the $I(V)$ characteristics are measured for both the cooling-down and heating-up sweep. The tested RTD has a diameter of $d = 23 \mu\text{m}$. Figure 4(a) shows the $j(V)$ characteristics measured at room temperature ($T = 295 \text{ K}$, orange spheres) and at $T = 4.2 \text{ K}$ (blue circles). From the $I(V)$ characteristics, j_{res} and j_{val} are extracted, averaged, and plotted vs temperature in Fig. 4(b), as black circles and red dots, respectively. The corresponding $PVCR = j_{\text{res}}/j_{\text{val}}$ is shown in Fig. 4(c) as a function of the temperature. Both j_{res} and j_{val} show nearly textbook-like

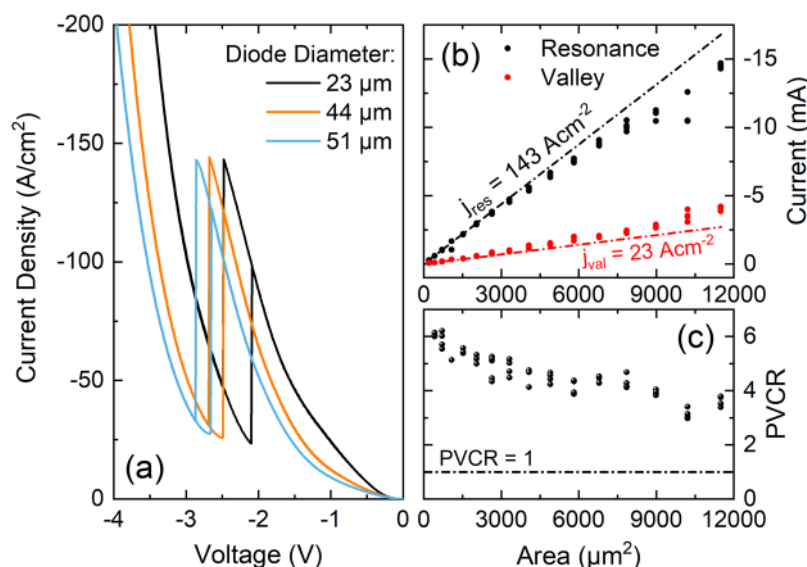


FIG. 3. (a) Diode area dependence. $I(V)$ characteristics measured for different diode diameters $d = 23 \mu\text{m}$, $d = 44 \mu\text{m}$, and $d = 51 \mu\text{m}$. (b) Resonance current (black dots) and valley current (red dots) measured for RTDs with different diameters. The dashed lines represent an extrapolation from the best measured diode. (c) Peak-to-valley current ratio vs diode area.

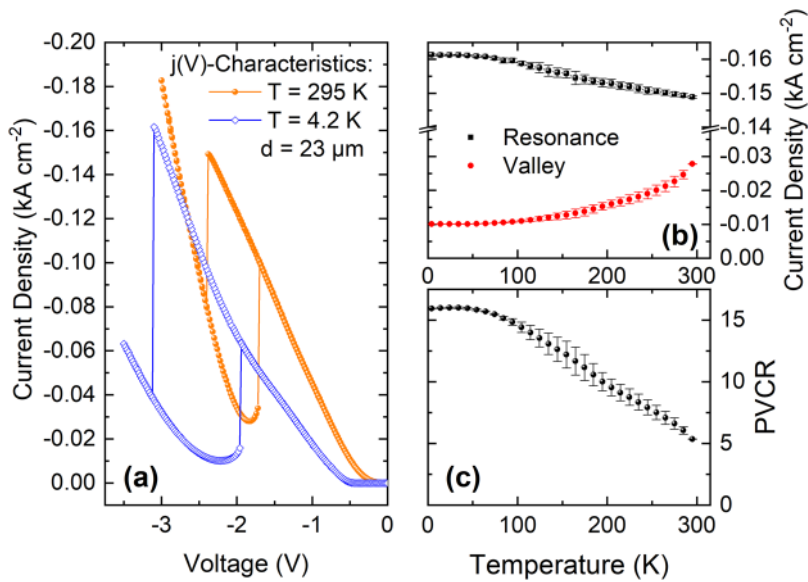


FIG. 4. Temperature dependence. (a) $j(V)$ characteristics taken at room temperature ($T = 295$ K, orange spheres) and at cryogenic temperatures ($T = 4.2$ K, blue circles). (b) Resonance and valley current densities (j_{res} , black squares) and (j_{val} , red dots) as a function of temperature. (c) Peak-to-valley current ratio as a function of temperature.

temperature dependence.⁴⁸ For temperatures below $T < 50$ K, resonance and valley current densities remain essentially constant with $j_{res} = 161$ A cm⁻² and $j_{val} = 10$ A cm⁻², and the $PVCR = 16$. For further increasing temperatures up to $T = 295$ K, the resonance current density decreases by 8% to $j_{res} = 149$ A cm⁻², whereas the valley current density increases to $j_{val} = 28$ A cm⁻², and the $PVCR = 5.4$. The decreasing j_{res} with increasing T can be attributed to increasing inelastic scattering,^{49,50} whereas the increase in valley current density can additionally be attributed to thermally activated tunneling.^{48,49,51,52}

In short, we have presented an extensive study on the optical and electrical properties of AlSb/GaInAsSb double barrier quantum well resonant tunneling diodes comprising the quaternary semiconductor $(\text{GaSb})_x(\text{InAs}_{0.91}\text{Sb}_{0.09})_{1-x}$ grown lattice-matched to GaSb as emitter, quantum well, and collector material. The optical properties have been studied by Fourier-transform photoluminescence spectroscopy. The pronounced single-peak PL emission with an Urbach parameter $E_U = 10$ meV indicates a direct bandgap semiconductor with high crystal quality and no miscibility issues. The composition-dependent bandgap energy suggests that Shim's model is well suited to describe the composition-dependent band alignments. Furthermore, we have demonstrated resonant tunneling of electrons across a large temperature spectrum from $T = 4$ K up to room temperature, with peak-to-valley current ratios of up to $PVCR = 16$ at cryogenic temperatures and $PVCR = 6.2$ at room temperature. Therefore, AlSb/GaInAsSb are promising candidates for optoelectronic applications in the mid-infrared spectral region that offer great design flexibility.

The authors are grateful for financial support from the State of Bavaria and the German Ministry of Education and Research (BMBF) via the national projects HIRT (Grant Nos. FKZ: 13XP5003A and 13XP5003B) and Photon-N (Grant No. FKZ: 13N15125). E.D.G.C. acknowledges financial support from

the Coordenação de Aperfeiçoamento de Pessoal de Nível Superior—Brasil (CAPES)—Finance Code 001. This project received funding from the European Union's Horizon 2020 research and innovation program under the Marie Skłodowska-Curie grant, Agreement No. 765426 (TeraApps).

The data that support the findings of this study are available from the corresponding author upon reasonable request.

REFERENCES

- C. R. Webster, P. R. Mahaffy, S. K. Atreya, G. J. Flesch, M. A. Mischna, P.-Y. Meslin, K. A. Farley, P. G. Conrad, L. E. Christensen, A. A. Pavlov, J. Martin-Torres, M.-P. Zorzano, T. H. McConnochie, T. Owen, J. L. Eigenbrode, D. P. Glavin, A. Steele, C. A. Malespin, P. D. Archer, B. Sutter, P. Coll, C. Freissinet, C. P. McKay, J. E. Moores, S. P. Schwenzer, J. C. Bridges, R. Navarro-Gonzalez, R. Gellert, and M. T. Lemmon, *Science* **347**, 415 (2015).
- C. S. Goldenstein, R. M. Spearrin, J. B. Jeffries, and R. K. Hanson, *Prog. Energy Combust. Sci.* **60**, 132 (2017).
- Z. Du, S. Zhang, J. Li, N. Gao, and K. Tong, *Appl. Sci.* **9**, 338 (2019).
- N. M. Israelsen, C. R. Petersen, A. Barh, D. Jain, M. Jensen, G. Hanneschläger, P. Tidemand-Lichtenberg, C. Pedersen, A. Podoleanu, and O. Bang, *Light: Sci. Appl.* **8**, 11 (2019).
- G. G. Taylor, D. Morozov, N. R. Gemell, K. Erotokritou, S. Miki, H. Terai, and R. H. Hadfield, *Opt. Express* **27**, 38147 (2019).
- K. J. Morse, R. J. S. Abraham, A. DeAbreu, C. Bowness, T. S. Richards, H. Riemann, N. V. Abrosimov, P. Becker, H.-J. Pohl, M. L. W. Thewalt, and S. Simmons, *Sci. Adv.* **3**, e1700930 (2017).
- L. M. Rosenfeld, D. A. Sulway, G. F. Sinclair, V. Anant, M. G. Thompson, J. G. Rarity, and J. W. Silverstone, "Mid-infrared quantum optics in silicon," [arXiv:1906.10158](https://arxiv.org/abs/1906.10158) [quant-ph] (2019).
- "Extending opportunities," *Nat. Photonics* **6**, 407 (2012).
- H. Kroemer, *Physica E* **20**, 196 (2004).
- B. R. Bennett, R. Magno, J. B. Boos, W. Kruppa, and M. G. Ancona, *Solid-State Electron.* **49**, 1875 (2005).
- G. K. Veerabhatran, S. Sprengel, A. Andrejew, and M.-C. Amann, *Appl. Phys. Lett.* **110**, 071104 (2017).

- ¹²A. N. Baranov and R. Teissier, *IEEE J. Sel. Top. Quantum Electron.* **21**, 85 (2015).
- ¹³I. Vurgaftman, R. Weih, M. Kamp, J. R. Meyer, C. L. Canedy, C. S. Kim, M. Kim, W. W. Bewley, C. D. Merritt, J. Abell, and S. Höfling, *J. Phys. D: Appl. Phys.* **48**, 123001 (2015).
- ¹⁴E. Tournié and L. Cerutti, *Mid-Infrared Optoelectronics: Materials, Devices, and Applications*, 1st ed. (Elsevier, 2019).
- ¹⁵A. B. Ikyo, I. P. Marko, K. Hild, A. R. Adams, S. Arafin, M. C. Amann, and S. J. Sweeney, *Sci. Rep.* **6**, 19595 (2016).
- ¹⁶L. Lei, L. Li, H. Lotfi, Y. Jiang, R. Q. Yang, M. B. Johnson, D. Lubyshev, Y. Qiu, J. M. Fastenau, and A. W. K. Liu, *Semicond. Sci. Technol.* **31**, 105014 (2016).
- ¹⁷K. Ryczko and G. Sęk, *Appl. Phys. Express* **11**, 012703 (2018).
- ¹⁸M. Motyka, G. Sęk, K. Ryczko, M. Dyksik, R. Weih, G. Patriarche, J. Misiewicz, M. Kamp, and S. Höfling, *Nanoscale Res. Lett.* **10**, 471 (2015).
- ¹⁹J.-L. Lazzari, F. De Anda, J. Nieto, H. Ait-Kaci, M. Mebarki, F. Chevrier, P. Christol, and A. Joullié, *AIP Conf. Proc.* **890**, 115–126 (2007).
- ²⁰J. E. Maslar, W. S. Hurst, and C. A. Wang, *J. Appl. Phys.* **106**, 123502 (2009).
- ²¹C. A. Wang, D. A. Shiau, R. K. Huang, C. T. Harris, and M. K. Connors, *J. Cryst. Growth* **261**, 379 (2004).
- ²²R. K. Huang, C. A. Wang, C. T. Harris, M. K. Connors, and D. A. Shiau, *J. Electron. Mater.* **33**, 1406 (2004).
- ²³R. Tsu and L. Esaki, *Appl. Phys. Lett.* **22**, 562 (1973).
- ²⁴L. L. Chang, L. Esaki, and R. Tsu, *Appl. Phys. Lett.* **24**, 593 (1974).
- ²⁵A. Pfenning, F. Hartmann, F. Langer, M. Kamp, S. Höfling, and L. Worschech, *Nanotechnology* **27**, 355202 (2016).
- ²⁶J. P. Sun, G. Haddad, P. Mazumder, and J. N. Schulman, *Proc. IEEE* **86**, 641 (1998).
- ²⁷J. Encomendero, F. A. Faria, S. M. Islam, V. Protasenko, S. Rouvimov, B. Sensale-Rodriguez, P. Fay, D. Jena, and H. G. Xing, *Phys. Rev. X* **7**, 041017 (2017).
- ²⁸E. Ozbay, D. M. Bloom, D. H. Chow, and J. N. Schulman, *IEEE Electron Device Lett.* **14**, 400 (1993).
- ²⁹E. R. Brown, J. R. Söderström, C. D. Parker, L. J. Mahoney, K. M. Molvar, and T. C. McGill, *Appl. Phys. Lett.* **58**, 2291 (1991).
- ³⁰J. R. Söderström, D. H. Chow, and T. C. McGill, *IEEE Electron Device Lett.* **11**, 27 (1990).
- ³¹J. L. Jimenez, X. Li, and W. I. Wang, *Appl. Phys. Lett.* **64**, 2127 (1994).
- ³²J. Jimenez, E. Mendez, X. Li, and W. Wang, *Phys. Rev. B* **52**, R5495 (1995).
- ³³S. Höfling, A. Pfenning, R. Weih, A. Ratajczak, F. Hartmann, G. Knebl, M. Kamp, and L. Worschech, *Proc. SPIE* **9973**, 997306 (2016).
- ³⁴F. Rothmayr, A. Pfenning, C. Kistner, J. Koeth, G. Knebl, A. Schade, S. Krueger, L. Worschech, F. Hartmann, and S. Höfling, *Appl. Phys. Lett.* **112**, 161107 (2018).
- ³⁵A. Pfenning, F. Hartmann, R. Weih, M. Emmerling, L. Worschech, and S. Höfling, *Adv. Opt. Mater.* **6**, 1800972 (2018).
- ³⁶K. Shim, *J. Appl. Phys.* **114**, 203703 (2013).
- ³⁷I. E. Gordon, L. S. Rothman, C. Hill, R. V. Kochanov, Y. Tan, P. F. Bernath, M. Birk, V. Boudon, A. Campargue, K. V. Chance, B. J. Drouin, J.-M. Flaud, R. R. Gamache, J. T. Hodges, D. Jacquemart, V. I. Perevalov, A. Perrin, K. P. Shine, M.-A. H. Smith, J. Tennyson, G. C. Toon, H. Tran, V. G. Tyuterev, A. Barbe, A. G. Császár, V. M. Devi, T. Furtenbacher, J. J. Harrison, J.-M. Hartmann, A. Jolly, T. J. Johnson, T. Karman, I. Kleiner, A. A. Kyuberis, J. Loos, O. M. Lyulin, S. T. Massie, S. N. Mikhailenko, N. Moazzen-Ahmadi, H. S. P. Müller, O. V. Naumenko, A. V. Nikitin, O. L. Polyansky, M. Rey, M. Rotger, S. W. Sharpe, K. Sung, E. Starikova, S. A. Tashkun, J. V. Auwera, G. Wagner, J. Wilzewski, P. Wcisło, S. Yu, and E. J. Zak, *J. Quant. Spectrosc. Radiat. Transfer* **203**, 3 (2017).
- ³⁸F. Urbach, *Phys. Rev.* **92**, 1324 (1953).
- ³⁹P. Van Mieghem, *Rev. Mod. Phys.* **64**, 755 (1992).
- ⁴⁰V. Rakovics, A. L. Tóth, B. Podór, C. Frigeri, J. Balázs, and Z. E. Horváth, *Mater. Sci. Eng. B* **91-92**, 83 (2002).
- ⁴¹A. Yildirim and J. P. Prineas, *J. Vac. Sci. Technol., B* **30**, 02B104 (2012).
- ⁴²I. Vurgaftman, J. R. Meyer, and L. R. Ram-Mohan, *J. Appl. Phys.* **89**, 5815 (2001).
- ⁴³A. Pfenning, G. Knebl, F. Hartmann, R. Weih, M. Meyer, A. Bader, M. Emmerling, L. Worschech, and S. Höfling, *Appl. Phys. Lett.* **111**, 171104 (2017).
- ⁴⁴A. Pfenning, G. Knebl, A. Schade, R. Weih, A. Bader, M. Meyer, S. Krüger, F. Rothmayr, C. Kistner, J. Koeth, M. Kamp, F. Hartmann, L. Worschech, and S. Höfling, “Infrared remote sensing and instrumentation XXVI,” *Proc. SPIE* **10765**, 107650U (2018).
- ⁴⁵K. Nomoto, K. Taira, T. Suzuki, I. Hase, H. Hiroshima, and M. Komuro, *Appl. Phys. Lett.* **70**, 2025 (1997).
- ⁴⁶A. Pfenning, G. Knebl, F. Hartmann, R. Weih, A. Bader, M. Emmerling, M. Kamp, S. Höfling, and L. Worschech, *Appl. Phys. Lett.* **110**, 033507 (2017).
- ⁴⁷T. A. Growden, D. F. Storm, E. M. Cornuelle, E. R. Brown, W. Zhang, B. P. Downey, J. A. Roussos, N. Cronk, L. B. Ruppalt, J. G. Champlain, P. R. Berger, and D. J. Meyer, *Appl. Phys. Lett.* **116**, 113501 (2020).
- ⁴⁸H. Mizuta and T. Tanoue, *The Physics and Applications of Resonant Tunneling Diodes* (Cambridge University Press, Cambridge, 2006).
- ⁴⁹Y. Fu, Q. Chen, M. Willander, H. Brugger, and U. Meiners, *J. Appl. Phys.* **74**, 1874 (1993).
- ⁵⁰N. Zou, Q. Chen, and M. Willander, *J. Appl. Phys.* **75**, 1829 (1994).
- ⁵¹L. de Saint Pol, O. Vanbesien, and D. Lippens, *Electron. Lett.* **26**, 342 (1990).
- ⁵²K. J. P. Jacobs, B. J. Stevens, R. Baba, O. Wada, T. Mukai, and R. A. Hogg, *AIP Adv.* **7**, 105316 (2017).